This is a repository copy of *Active thermal management for Interior Permanent Magnet Synchronous Machine (IPMSM) drives based on model predictive control*.

White Rose Research Online URL for this paper:
http://eprints.whiterose.ac.uk/131330/

Version: Accepted Version

---

**Article:**

Sun, T., Wang, J., Griffo, A. orcid.org/0000-0001-5642-2921 et al. (1 more author) (2018) Active thermal management for Interior Permanent Magnet Synchronous Machine (IPMSM) drives based on model predictive control. IEEE Transactions on Industry Applications, 54 (5). pp. 4506-4514. ISSN 0093-9994

https://doi.org/10.1109/TIA.2018.2843350

---

© 2018 IEEE. This is an author produced version of a paper subsequently published in IEEE Transactions on Industry Applications. Uploaded in accordance with the publisher's self-archiving policy. Personal use of this material is permitted. Permission from IEEE must be obtained for all other uses, in any current or future media, including reprinting/republishing this material for advertising or promotional purposes, creating new collective works, for resale or redistribution to servers or lists, or reuse of any copyrighted component of this work in other works.

**Reuse**

Items deposited in White Rose Research Online are protected by copyright, with all rights reserved unless indicated otherwise. They may be downloaded and/or printed for private study, or other acts as permitted by national copyright laws. The publisher or other rights holders may allow further reproduction and re-use of the full text version. This is indicated by the licence information on the White Rose Research Online record for the item.

**Takedown**

If you consider content in White Rose Research Online to be in breach of UK law, please notify us by emailing eprints@whiterose.ac.uk including the URL of the record and the reason for the withdrawal request.

eprints@whiterose.ac.uk
https://eprints.whiterose.ac.uk/

# Active Thermal Management for Interior Permanent Magnet Synchronous Machine (IPMSM) Drives Based on Model Predictive Control

Tianfu Sun, *Member*, *IEEE*, Jiabin Wang, *Senior Member*, *IEEE*, Antonio Griffo *Member*, *IEEE*, Bhaskar Sen *Member*, *IEEE*

*Abstract*—**This paper proposes an active thermal management scheme for Interior Permanent Magnet Synchronous Machine (IPMSM) drives based on the model predictive control concept. The proposed control scheme can adaptively set torque limit based on the thermal state of the machine to limit the machine winding and end-winding temperatures. The proposed control scheme is assessed by experiments on a laboratory machine drive system and simulated for traction drives over Worldwide Harmonized Light-duty Test Cycle (WLTC). Compared with conventional traction control scheme, the proposed scheme can effectively reduce peak temperature and hence thermal stress of the machine for improving its lifetime.**

***Keywords***— ***Temperature control; motor thermal model; model predictive control; machine drive; IPMSM***

## I. INTRODUCTION

Permanent magnet (PM) machines have increasingly been employed in a variety of applications ranging from automotive, aerospace and industrial automation to renewable power generation [1], [2]. In many these applications, PM machines often have to operate under transient conditions that can vary significantly in terms of cooling, ambient temperature, and power/torque output [3]. Consequently, the winding, end-winding and magnet temperatures of the machines can change over a very wide range.

Although it is possible to predict machine thermal behaviour against the worst operating conditions and to take design measures to avoid overheating [4], these may lead to overly conservative designs or to underestimate real operating conditions which may cause excessive thermal stress. It is well known that the insulation lifetime of machine winding is very sensitive to cumulative thermal stress and temperature cycling as the frequent overheating can lead to significant reductions in lifetime and reliability. For PM machines, overheating may result in partial demagnetisation and this would further increase the thermal stress as torque capabilities reduces and hence current increases for the same load torque. The vicious circle may continue and result in more severe consequence.

It is, therefore, essential to manage the thermal stress of PM machines in real operating conditions. A constant current limit is often imposed on machine drives to prevent overheating [5]. However, this does not account the thermal state of the machine in real operation. If the machine temperature is relatively low, the limit can be relaxed to allow for higher output torque or power. On the other hand, if the machine temperature is already very high, the current limit will not be able to prevent overheating. In some applications, temperature sensors are used to disable the machine drives if the machine or inverter temperature exceeds a predefined limit, this leads to complete loss of the machine output torque/power and potentially uncontrolled rectification, which is not acceptable in many applications.

Various attempts have been made to improve thermal management of electrical machines. In applications where a large contribution to the machine torque is due to acceleration and deceleration, a trade-off between drive control effort (motor torque) and performance (position or speed tracking error) may be possible [6]. When the machine operates at high temperature, relaxation in drive performance requirements makes it possible to reduce control effort (torque) and hence machine temperature. The trade-off can be formulated in the form of the linear quadratic regulator (LQR) based on measured or estimated machine temperature [6]. However, the technique is effective only if the majority of the torque is for acceleration/deceleration. In [7], model predictive control (MPC) was adopted to estimate the current limit of induction machines to keep temperature within predefined constraints over a specified prediction horizon based on a lumped-parameter thermal network (LPTN) model [8], [9]. However, the relatively complex lumped-parameter thermal model increases the computation load. In addition, the experimental results indicated that the thermal management scheme leads to a long-time estimation error which leads to further drift with time [7]. In [10], a model predictive thermal overload control scheme was proposed to actively control the temperatures of switched reluctance motors based on a 41 nodes thermal model proposed in [11]. This control scheme also suffers from the excessive computational load and cannot update thermal parameters according to the operating conditions.

---

The work is partly funded by the UK Engineering and Physics Research Council (EPSRC) under EP/K034987/1 [Integrated Drives theme]

Manuscript received September 20, 2017; revised January 16, 2018, April 27, 2018 and May 17, 2018; accepted May 18, 2018. (*Corresponding author: Tianfu Sun*)

Tianfu Sun is with Shenzhen Institutes of Advanced Technology, Chinese Academy of Sciences, Shenzhen, China (e-mail: tianfu.sun@foxmail.com).

Jiabin Wang, Antonio Griffo and Bhaskar Sen are with the Department of Electronic and Electrical Engineering, University of Sheffield, Sheffield, S1 3JD, UK (e-mail: j.b.wang@sheffield.ac.uk, a.griffo@sheffield.ac.uk, bsen.ee@gmail.com).

The work reported in this paper was performed at the University of Sheffield, UK, where Tianfu Sun was a Postdoctoral Research Fellow.

In this paper, a thermal management scheme based on a three-node-lumped-parameter thermal model for interior permanent magnet machine drive is proposed. The proposed control scheme combines the maximum torque per ampere (MTPA) control scheme [12] and voltage-constrained MTPA (VCMTPA) control scheme [13] with the model predictive control based on a 3-node-lumped-parameter thermal network model [14] to generate an adaptive torque limit according to the thermal state of the machine in order to reduce its thermal stress. The proposed thermal control scheme is verified by simulations and experiments.

The rest of the paper is organized as follows. Section II describes the active thermal management strategy for IPM machines based on a three-node thermal network. Section III presents simulations of the proposed thermal management strategy for a traction drive over WLTC cycle and discusses the results. Section IV presents experimental results from testing of a prototype IPM drive in the laboratory. The conclusions are drawn in section V.

## II. ACTIVE THERMAL MANAGEMENT

### A. *Active Thermal Management Scheme*

The schematic of the active thermal management scheme is shown in Fig. 1. The innermost is a current control loop where the d- and q-axis currents are controlled by two PI current controllers whose inputs are the error between the measured currents and reference currents. The outputs of the current controller are the reference voltages with decoupling compensation and they are fed to the inverter. The outer loop is the speed control loop where the reference speed and measured speed are fed to a PI speed controller to generate the reference torque command, $T_e^*$. In order to limit the motor temperature, the reference torque is limited by the proposed MPC control block in Fig. 1 and the limited reference torque ($T_{e\_lim}$) is fed to a look-up table to generate the d- and q-axis current commands for MTPA or VCMTPA control.

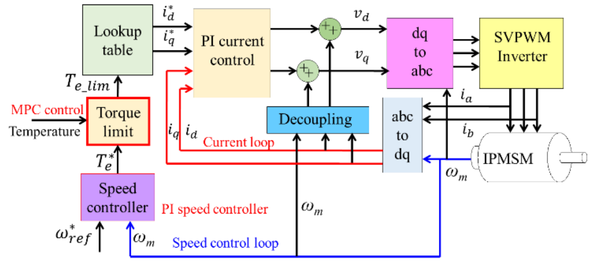
Lookup table
$i_d^*$
$i_q^*$
PI current control
$v_d$
$v_q$
dq to abc
SVPWM Inverter
$T_{e\_lim}$
MPC control
Temperature
Torque limit
$i_q$ $i_d$
Current loop
Decoupling
abc to dq
$i_a$
$i_b$
IPMSM
$\omega_m$
$T_e^*$
Speed controller
PI speed controller
$\omega_m$
$\omega_{ref}^*$
$\omega_m$
Speed control loop

Fig. 1. Schematic of the motor control loops

As shown in Fig. 1, $T_{e\_lim}$ is generated by an MPC control block to prevent the motor temperature from exceeding the maximum reference temperature. In this paper, the MPC control is based on a 3-node-lumped-parameter thermal network. The overall schematic of the model predictive thermal management based on the 3-node thermal network is shown in Fig. 2.

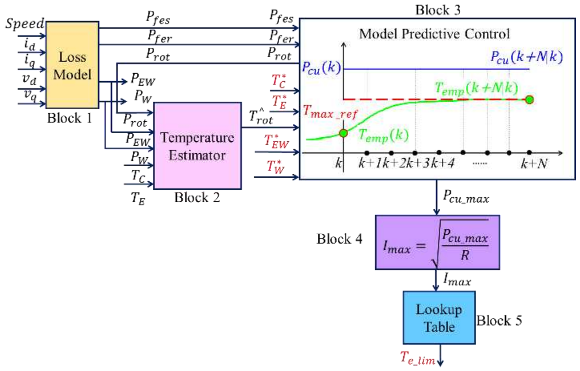
Speed
$i_d$
$i_q$
$v_d$
$v_q$
Loss Model
Block 1
$P_{fes}$
$P_{fer}$
$P_{rot}$
$P_{EW}$
$P_W$
$P_{rot}$
$P_{EW}$
$P_W$
$T_C$
$T_E$
Temperature Estimator
Block 2
$P_{fes}$
$P_{fer}$
$P_{rot}$
$T_C^*$
$T_E^*$
$\hat{T}_{rot}$
$T_{EW}^*$
$T_W^*$
Block 3
Model Predictive Control
$P_{cu}(k)$
$P_{cu}(k+N|k)$
$T_{emp}(k+N|k)$
$T_{max\_ref}$
$T_{emp}(k)$
$k$ $k+1$ $k+2$ $k+3$ $k+4$ ...... $k+N$
$P_{cu\_max}$
Block 4
$I_{max} = \sqrt{\frac{P_{cu\_max}}{R}}$
$I_{max}$
Lookup Table
Block 5
$T_{e\_lim}$

Fig. 2. The overall schematic of the 3 nodes lumped model MPC based active thermal management.

As can be seen in Fig. 2, the MPC-based active thermal management mainly consists of five blocks. The first block is the loss model which estimates the winding copper loss ($P_W$), end-winding copper loss ($P_{EW}$), the rotor loss ($P_{rot}$), the iron losses in stator ($P_{fes}$) and rotor ($P_{fer}$) under a given operating condition. The second block is the temperature estimator which estimates the rotor temperature ( $T_{rot}$ ) based on ambient temperature ($T_E$), coolant temperature ($T_C$) and the estimated power losses from the loss model. The third block is the model predictive control which calculates the maximum copper loss ($P_{cu\_max}$) to prevent the motor temperature from exceeding the maximum reference temperature based on the measured winding, end-winding, ambient and coolant temperatures, and the estimated rotor temperature as well as the estimated losses. The maximum copper loss ($P_{cu\_max}$) is fed to a look-up table in the fifth block to generate the adaptive torque limit for MTPA or VCMTPA control under the temperature constraint. The details of each block will be described below.

### B. *Power Loss Model*

The losses in the motor can generally be divided into the iron loss, mechanical loss, copper loss and stray loss. Among these losses, the copper loss, iron loss, and the mechanical and magnetic losses are the main contributors to the winding, end-winding, and rotor temperature increases.

The copper losses are caused by the current flow in the stator resistance. The stator resistance can be calculated by (1):

$$R_S = R_{S0}[1 + \alpha(T_W^* - T_0)] \tag{1}$$

where $R_{S0}$ is the stator resistance at temperature $T_0$; $\alpha$ is the temperature coefficient of the resistance; $T_W^*$ is the instantaneous winding temperature. The copper losses can be expressed as follows:

$$P_{cu} = R_S\left(i_d^2 + i_q^2\right) \tag{2}$$

where, $i_d$ and $i_q$ are the d- and q-axis currents, respectively. The iron losses comprise hysteresis and eddy current loss components and they are calculated by the model described in [15]. The iron loss can be calculated by the component associated with the voltage magnitude in (3) and the component associated with the demagnetising field in (5) :

$$P_{fe}^{OC} = \alpha_1 \frac{V_m}{2\pi\Psi_m} + \alpha_2 \left(\frac{V_m}{2\pi\Psi_m}\right)^2 + \alpha_3 \left(\frac{V_m}{2\pi\Psi_m}\right)^{1.5} \tag{3}$$

where $V_m$ is the voltage magnitude. ($\alpha_1$, $\alpha_2$, $\alpha_3$) are losses coefficients related to machine characteristics in open-circuit which are extracted from finite element (FE) analysis. $\Psi_m$ is the flux-linkage due to permanent magnets. $V_m$ in (3) can be evaluated by (4). The $\Psi_d$ and $\Psi_q$ in (4) are obtained by FE analysis and stored in look-up tables which relate the stator flux linkages with stator currents.

$$|V_m| = \omega_e \sqrt{\Psi_d^2 + \Psi_d^2} \tag{4}$$

$$P_{fe}^{SC} = b_1 \frac{V_{d\alpha}}{2\pi\Psi_m} + b_2 \left(\frac{V_{d\alpha}}{2\pi\Psi_m}\right)^2 + b_3 \left(\frac{V_{d\alpha}}{2\pi\Psi_m}\right)^{1.5} \tag{5}$$

The voltage associated with the demagnetising field $V_{d\alpha}$ is equal to:

$$|V_{d\alpha}| = |\omega_e(\Psi_d - \Psi_m)| \tag{6}$$

The coefficients ($b_1$, $b_2$, $b_3$) are obtained by FE analysis of the iron loss in short-circuit conditions. The total iron loss at a given operation condition is the sum of $P_{fe}^{OC}$ and $P_{fe}^{SC}$. More details on the iron loss calculation can be found in [16].

It is worth noting that machine temperature variations may influence some variables in the iron loss calculations above. Therefore, taking into account the thermal effects into the iron losses calculation [17] may give a better temperature estimation.

After the copper loss and iron loss are calculated, the power losses distribution at windings, end-windings, and rotor can be obtained by (7) to (9):

$$P_W = aP_{cu} + P_{fes} \tag{7}$$

$$P_{EW} = bP_{cu} \tag{8}$$

$$P_{rot} = P_{fer} + P_{mech} + P_{mag} \tag{9}$$

where, $P_{fes}$ is the stator iron losses, $P_{fer}$ is the rotor iron losses and they can be calculated separately from the general equations (3) and (5) by only changing the coefficients. The $P_{mech}$ is the mechanical losses which can be calculated from bearing friction. The magnet loss $P_{mag}$ as a function of rotor speed and stator currents are obtained from FE and it is lumped into the rotor loss. For the machine under consideration, the magnet loss is quite small because the magnets are buried in the rotor lamination which shields the high frequency magnetic field seen by the magnets. The coefficients $a$ and $b$ are parameters dependent on machine active length and end winding length.

### C. Three Nodes Lumped Parameter Thermal Network

For both the temperature estimator block and the model predictive control block in Fig. 2, a motor thermal model is needed. In this section, a low-order LPTN model [14], [18] is adopted as shown in Fig. 3. The temperatures of the winding, end-winding and rotor are represented by $T_W$, $T_{EW}$ and $T_{rot}$, respectively, and their thermal capacitances are denoted by $C_W$, $C_{EW}$, and $C_{rot}$. The power losses ($P_W$, $P_{EW}$, and $P_{rot}$) are injected in parallel at each node. The three nodes are interconnected through thermal resistances ($R_{W-EW}$, $R_{W-rot}$, $R_{W-C}$, $R_{rot-E}$), as shown in Fig. 3. This model is simple for computation while preserving the main motor thermal characteristics.

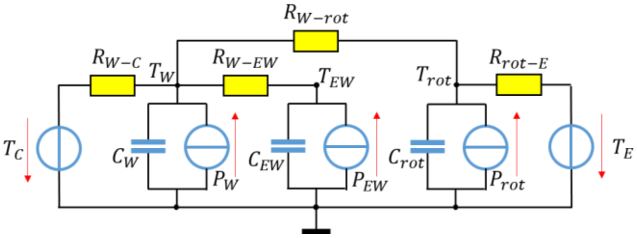

Fig. 3. Lumped parameter thermal network model.

The state space equations of the thermal network shown in Fig. 3 are listed in (10)-(16):

$$\begin{bmatrix} \dot{T}_W \\ \dot{T}_{EW} \\ \dot{T}_{rot} \end{bmatrix} = A \cdot \begin{bmatrix} T_W \\ T_{EW} \\ T_{rot} \end{bmatrix} + B \cdot \begin{bmatrix} P_W \\ P_{EW} \\ P_{rot} \\ T_C \\ T_E \end{bmatrix} \tag{10}$$

where:

$$A = \begin{bmatrix} C_W & 0 & 0 \\ 0 & C_{EW} & 0 \\ 0 & 0 & C_{rot} \end{bmatrix}^{-1} \begin{bmatrix} a_{11} & a_{12} & a_{13} \\ a_{21} & a_{22} & 0 \\ a_{31} & 0 & a_{33} \end{bmatrix} \tag{11}$$

$$a_{11} = -\left(\frac{1}{R_{WC}} + \frac{1}{R_{W-EW}} + \frac{1}{R_{W-rot}}\right) \tag{12}$$

$$a_{12} = a_{21} = -a_{22} = \frac{1}{R_{W-EW}} \tag{13}$$

$$a_{13} = a_{31} = \frac{1}{R_{W-rot}} \tag{14}$$

$$a_{33} = -\left(\frac{1}{R_{W-rot}} + \frac{1}{R_{rot-E}}\right) \tag{15}$$

$$B = \begin{bmatrix} b_{11} & 0 & 0 & b_{14} & 0 \\ 0 & b_{22} & 0 & 0 & 0 \\ 0 & 0 & b_{33} & 0 & b_{35} \end{bmatrix} \tag{16}$$

$$b_{11} = 1/C_W \quad (17) \qquad b_{22} = 1/C_{EW} \quad (18)$$

$$b_{33} = 1/C_{rot} \quad (19) \qquad b_{14} = 1/(C_W R_{WC}) \quad (20)$$

$$b_{35} = 1/(C_{rot} R_{rot-E}) \tag{21}$$

$T_C$ and $T_E$ are the coolant temperature and ambient temperatures, respectively. $P_W$, $P_{EW}$ and $P_{rot}$ are the losses associated with the active part of the stator, the end-winding and the rotor, respectively, and they are calculated by (7)-(9).

Since the iron loss in a PM machine depends more strongly on motor speed than on the current, it can be separated from the copper loss. Therefore, matrix $B$ in (10) can be divided into $B_{con}$ and $B_{var}$ as shown in (22).

$$\begin{bmatrix} \dot{T}_W \\ \dot{T}_{EW} \\ \dot{T}_{rot} \end{bmatrix} = A \cdot \begin{bmatrix} T_W \\ T_{EW} \\ T_{rot} \end{bmatrix} + B_{con} \cdot \begin{bmatrix} P_{fes} \\ P_{fer} \\ P_{mech} \\ T_C \\ T_E \end{bmatrix} + B_{var} P_{cu} \tag{22}$$

$$B_{con} = \begin{bmatrix} b_{con11} & 0 & 0 & b_{con14} & 0 \\ 0 & 0 & 0 & 0 & 0 \\ 0 & b_{con32} & b_{con33} & 0 & b_{con35} \end{bmatrix} \quad (23)$$

$$b_{con11} = 1/C_W \quad (24)$$

$$b_{con14} = 1/(C_W R_{W-C}) \quad (25)$$

$$b_{con32} = b_{con33} = 1/C_{rot} \quad (26)$$

$$b_{con35} = 1/(C_{rot} R_{rot-E}) \quad (27)$$

$$B_{var} = \begin{bmatrix} a/C_W \\ b/C_{EW} \\ 0 \end{bmatrix} \quad (28)$$

Based on (22), the motor winding, end-winding temperatures, and the rotor temperature can be predicted as described in the following section.

### D. Motor Temperature Estimator

By discretising (22), the temperature vector at $k^{th}$ time step can be predicted by (29).

$$\begin{bmatrix} T_W(k) \\ T_{EW}(k) \\ T_{rot}(k) \end{bmatrix} = A_d \cdot \begin{bmatrix} T_W(k-1) \\ T_{EW}(k-1) \\ T_{rot}(k-1) \end{bmatrix} + B_{con\_d} \cdot \begin{bmatrix} P_{fes} \\ P_{fer} \\ P_{mech} \\ T_C \\ T_E \end{bmatrix} + B_{var\_d} P_{cu} \quad (29)$$

Where $A_d$ , $B_{con\_d}$, $B_{var\_d}$ are the discretized forms of $A$, $B_{con}$, and $B_{var}$ in (22). Since $P_{fes}$, $P_{fer}$ can be calculated by (3) and (5), $P_{mech}$ can be calculated from bearing friction and $T_C$ and $T_E$ are known, the motor winding temperature, end-winding temperature and rotor temperature can be estimated based on the temperatures estimated at the previous time step.

### E. MPC Based Active Thermal Management

Equation (29) provides the means of predicting motor temperatures over one time step; hence, by repeating the prediction for a number of steps, it is possible to predict the copper loss over a specified prediction horizon. According to (29), the future thermal state vector (temperature vector) after *N* time steps can be formulated by (30) through iteration where $P_{cu}(k+j)$ is the copper loss at the $j^{th}$ time step ($0<j<N-1$).

$$\vec{T}(k+N) = \begin{bmatrix} T_W(k+N) \\ T_{EW}(k+N) \\ T_{rot}(k+N) \end{bmatrix} = X + Y_P \quad (30)$$

$$X = A_d^N \cdot \begin{bmatrix} T_W(k) \\ T_{EW}(k) \\ T_{rot}(k) \end{bmatrix} + \sum_{j=0}^{N-1} A_d^{N-j-1} \cdot B_{con\_d} \cdot \begin{bmatrix} P_{fes} \\ P_{fer} \\ P_{mech} \\ T_C \\ T_E \end{bmatrix} \quad (31)$$

$$Y_P = \sum_{j=0}^{N-1} A_d^{N-j-1} \cdot B_{var\_d} \cdot P_{cu}(k+j) \quad (32)$$

Since the future motor speed variation is unknown over the prediction horizon, the iron loss is assumed to be the value at the $k^{th}$ time step and does not change over the *N* steps of the prediction horizon. In this way, for each time step $k$, the predicted temperature vector at the end of the prediction horizon is updated for the new value of $(k + N)$ based on the temperature vector of the $k^{th}$ time step and (30). The thermal model parameters of (30) are also updated from look-up tables in each time step $k$ based on operating conditions.

By employing a parameter identification technique, the thermal resistances and capacitances of the three-node model can be obtained either from experimental data or simulated data with a sophisticated model (lumped parameter or FE) for different cooling schemes. The degree of the model fitting to these data can be used to determine if the model structure should be changed or not for a given cooling scheme. The model can also cope with changes in the cooling condition during operation. The machine under study in this paper is an air-cooled motor designed for EV traction. Its cooling condition is dependent on vehicle speed. Hence the model parameters can be identified at a given set of speeds and used in a look-up table. Similar treatment may be employed for other cooling schemes to account changes in cooling conditions. Since the ambient temperature and coolant temperature vary slowly and do not change significantly during the short prediction horizon, the $T_C$ and $T_E$ can be measured by temperature sensors and assumed as constant during the *N* steps.

It is worth noting that the temperatures at the three nodes of the thermal model may closely represent the hotspot temperatures of the active winding, the end-winding, and the rotor if the parameters of the model are identified from the measured or simulated temperatures close to the hotspot temperatures. The differences between the model-predicted temperatures and the actual hotspot temperatures can be assessed by more sophisticated thermal model or 3D FEA. And a safety margin may be considered by setting the actively managed temperature limits.

### F. Maximum Copper Loss Calculation

By employing the model predictive control concept [10], the optimal maximum permissible copper loss sequence $P_{cu\_max}$ can be obtained by letting the predicted temperature vector at the end of the predictive horizon ($\vec{T}(k+N)$ in (30)) equal the maximum permissible temperature vector $\vec{T}_{max}$ . Therefore, based on (30), the maximum permissible copper loss sequence can be calculated by minimizing the cost function in (33) :

$$J(N) = \sum_{j=0}^{N} \left\| \vec{T}(k+j|k) - \vec{T}_{max} \right\|^2 \quad (33)$$

$\vec{T}(k+j|k)$ is the predicted motor temperature at the $j^{th}$ time step within the *N* time steps of prediction. The cost function can be further simplified based on the following assumptions: Since in most applications it is not possible to know the future load condition over the prediction horizon, the maximum permissible copper loss is assumed to be constant over the prediction horizon [9]. Consequently, the motor temperatures increase or decrease monotonically. Therefore, only the temperature at the end of the prediction horizon needs to be considered. The cost function in (33) can be simplified in (34).

$$J(N) = \left\| \vec{T}(k+N|k) - \vec{T}_{max} \right\|^2$$

$$= \left(\vec{T}(k+N|k) - \vec{T}_{max}\right)^T \cdot \left(\vec{T}(k+N|k) - \vec{T}_{max}\right) \quad (34)$$

Where the superscript $T$ denotes vector transposition. The maximum permissible copper loss can be obtained by letting $\partial J(N)/\partial P_{cu} = 0$ and the result is given in (35).

$$P_{cu\_max} = (Y^T \cdot Y)^{-1} \cdot Y^T \cdot \left(\vec{T}_{max} - X\right) \quad (35)$$

where $Y$ is given by

$$Y = \sum_{j=0}^{N-1} A_d^{N-j-1} \cdot B_{var\_d} \quad (36)$$

$P_{cu\_max}$ is calculated at every time step when the MPC output is updated. Once $P_{cu\_max}$ is obtained, the maximum current amplitude can be set according to (37).

$$I_{max} = \sqrt{\frac{P_{cu\_max}}{R_S(k)}} \quad (37)$$

The predicted maximum current amplitude is further fed to the look-up table to obtain the maximum torque limit, $T_{e\_lim}$. In this way, the torque limit is changed adaptively according to thermal state of the machine. It is worth noting that $X$ obtained in (31) is calculated based on $T_W(k)$, $T_{EW}(k)$, $T_{rot}(k)$. The $T_W(k)$ and $T_{EW}(k)$ may be obtained by temperature sensors embedded in the winding and end-winding. $T_{rot}(k)$ can be obtained by the temperature estimator in Fig. 2 or set as a constant equals to the maximum magnet temperature reference. In the latter case, (35) will minimize only the differences between the winding and end-winding temperatures and their respective limits. Some methods have been proposed for measuring the rotor temperature directly using e.g. wireless sensors [19], [20]. If these are employed, the $T_{rot}(k)$ can be set as the measured temperature.

## III. SIMULATION STUDY

To assess the performance of the proposed active thermal management scheme, simulations have been performed based on a 10 kW IPMSM drive designed for wide constant power operation in traction applications. The machine specification is given in Table I.

TABLE I. IPMSM PARAMETERS

| | |
|---|---|
| Number of pole-pairs | 3 |
| Phase resistance | 51.2 mΩ |
| Continuous/Maximum current | 58.5/118 A |
| Peak power at base speed | 10 kW |
| DC link voltage | 120 V |
| Based/maximum speed | 1350/4500 rpm |
| Continuous/peak torque | 35.5/70 Nm |
| Peak power at maximum speed | 7 kW |

The thermal behaviour of the machine in the simulation was represented by a 48 nodes high fidelity computationally efficient electro-thermally coupled model [17]. Thus, the effects of temperature on the loss components and torque were fully accounted for. Simulations of different torque and speed were performed based on this model and the variations of $P_W$, $P_{EW}$, $P_{rot}$, $T_W$, $T_{EW}$, $T_{rot}$ with time are recorded. Because the motor thermal characteristics may vary with rotor speed, the parameters of the 3-node thermal network at different rotor speed were identified respectively and stored in look-up tables. The identification procedure is similar to the one reported in [21]. The parameter identification for the three-node-lumped thermal model was performed using the MATLAB parameter estimation tool with $P_W$, $P_{EW}$, $P_{rot}$ set as the inputs and $T_W$, $T_{EW}$, $T_{rot}$ set as the output. It worth noting that since the temperatures vary inside the rotor, winding and end winding, the hot-spot temperatures of winding, end winding and rotor obtained by simulations or experiments were recorded as the $T_W$, $T_{EW}$, $T_{rot}$, respectively. [19], [20] proposed methods to measure rotor temperature, however, the parameter identifications for the three-node-lumped thermal model in this paper are based on the $T_{rot}$ obtained by simulations of the 48 nodes electro-thermally coupled model. The accuracy of the model is verified against the experimentally measured winding temperature as illustrated in Fig. 4.

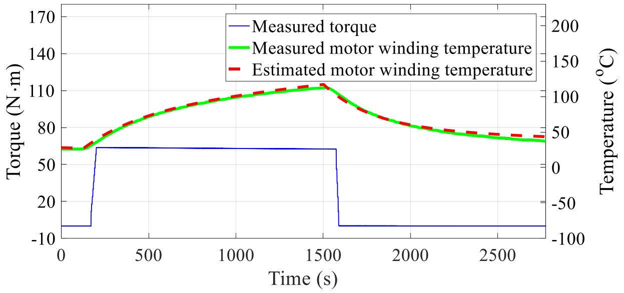

Fig. 4. The measured torque, measured motor winding temperature and estimated motor winding temperature.

The proposed active thermal management scheme has been simulated when the drive was employed in a distributed traction for a micro electric vehicle (sub-segment A class). The mass of the micro electric vehicle in the simulation was deliberately set much larger than its rated value to make the motor generate more heat during the acceleration and deceleration to highlight the characteristics of the proposed control method. Simulations were performed against the Worldwide Harmonized Light Vehicles Test Cycle (WLTC) on a 0° gradient slope. To guarantee the braking performance, the torque limit imposed by the active thermal management scheme was disabled when the reference torque was negative. The simulation time step of the MPC was set to 10 s, and the number of steps in the prediction horizon was set to 10. The ambient temperature was set at 45 °C. The torque command was generated by a PI speed controller so that the vehicle speed follows the WLTC. Since the current loop in Fig. 1 is much faster than the motor thermal response, the current loop dynamic was neglected in the simulation. The maximum reference temperature was set at 135 °C so that the winding temperature and magnet temperature would not exceed their insulation class and grade limits. In order to reach cyclic temperature steady state, the simulation was performed over 10 WLTC cycles and the resultant winding and magnet temperatures together with the maximum reference temperature are shown in Fig. 5.

Fig. 6 shows the vehicle speed response in the first and last WLTC cycles. For the purpose of comparison, the speed responses when the active thermal management was not activated are also shown. The corresponding torque references, actual torques and torque limiting profiles generated from the active thermal management are shown in Fig. 7. As can be seen from Fig. 6 and Fig. 7, the vehicle speed followed the WLTC profile quite well in the first cycle when the motor winding temperature was lower than the reference, and the torque limit profile shown in Fig. 7 (a) generated by the active thermal management was greater than the reference torque. As the motor temperature continued to increase under this adverse driving condition, the adaptive torque limit generated by the active thermal management shown in Fig. 7 (b) was imposed on the traction system to maintain the winding and end-winding temperature close to the reference maximum of 135 °C. As mentioned above, in order to control the temperatures and guarantee the braking performance, the actual torque was only limited by the active thermal management scheme when torque demand was positive. Consequently, the vehicle speed deviated from the WLTC. The speed deviation from the WLTC is clearly seen in Fig. 6 (b). Therefore, the active thermal management is a trade-off between the drive performance (speed tracking accuracy in this case) and the machine thermal states to maintain the temperatures around the maximum reference temperature. In the case of electric vehicle traction, this trade-off is worthwhile for preserving the lifetime and safety of the traction system. It is worth noting that at between t=$1.78 \times 10^4$ s and $1.79 \times 10^4$ s in Fig. 7(b), the torque limit dropped approximately to zero, forcing the actual torque also approximately to zero. This was due to the fact that the vehicle mass was set much higher than the rated value in the simulation. This would be avoided during powertrain design. For this extreme condition, whether the torque limit imposed by the active thermal management scheme should be disabled or not can be decided by the vehicle control unit (VCU) according to a comprehensive analysis of the data obtained from sensors on the vehicle body to guarantee driver's safety.

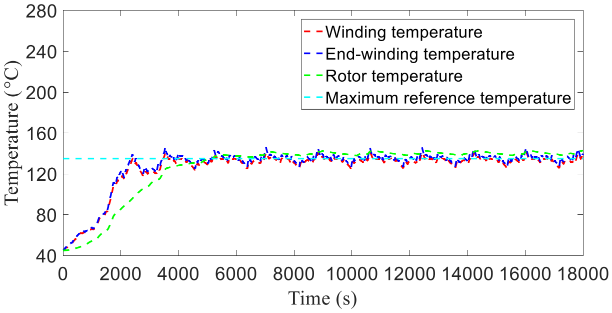

Fig. 5. The winding, end-winding and magnet temperatures.

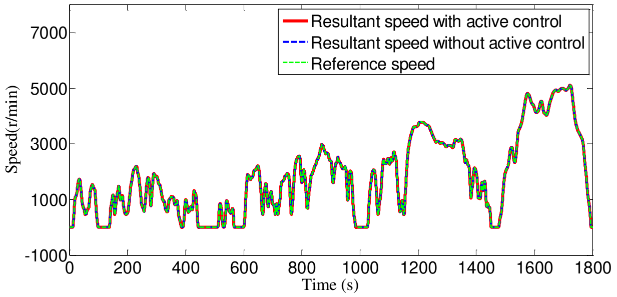

(a) First cycle

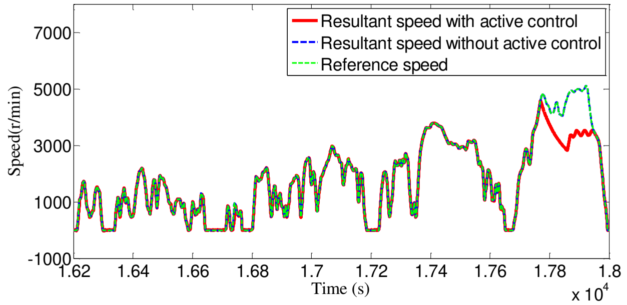

(b) Last cycle

Fig. 6. WLTC reference speed and actual speed with active thermal management.

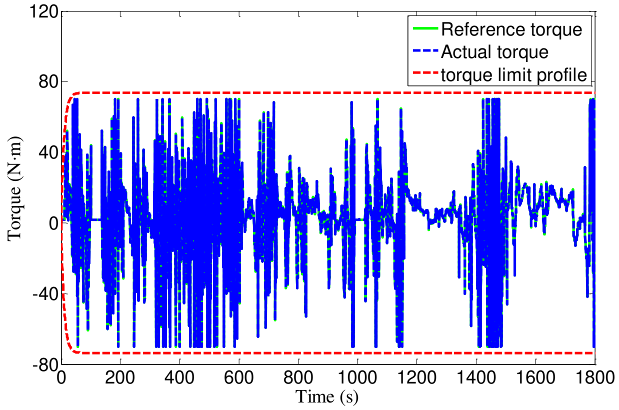

(a) First cycle

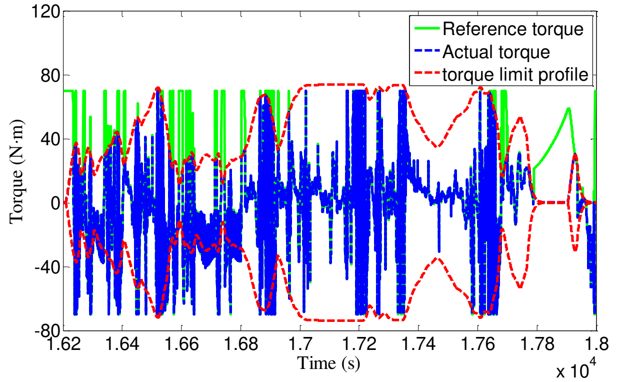

(b) Last cycle

Fig. 7. Reference torque, Adaptive torque limiting profile and the actual torque.

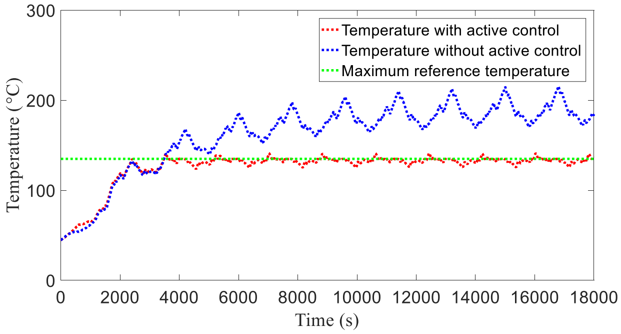

Fig. 8. Comparison between winding temperatures with and without active thermal management.

The comparison of the resultant winding temperatures over the driving cycles with and without the active temperature control is shown in Fig. 8. As can be seen, due to the active thermal management, the winding temperatures were controlled close to the maximum reference temperature (135 °C). The relatively small deviation was due to the assumptions made to simplify the cost function in (34). In contrast, the resultant temperature without active temperature control was much higher than the maximum reference temperature, and the peak temperature was over 200 °C. Given that the average life expectancy of winding insulation is reduced approximately by half for every 10 °C rise in temperature [6], the temperature difference shown in Fig. 8 will significantly affect the lifetime of the motor winding when the excessive winding temperature is not managed with the proposed active temperature management scheme.

## IV. EXPERIMENTAL RESULTS

In order to validate the active thermal management method discussed above, experiments were performed based on the 10 kW IPMSM described in section III with the test rig shown in Fig. 9. The active thermal management scheme in conjunction with field-oriented control operated in torque control mode was implemented in the drive controller while the machine is loaded by a dynamometer in speed control mode. A high precision torque transducer measured the resultant torque. The ambient temperature was regulated by the air conditioning system of the test cell to 23 °C. The winding and end-winding temperatures were measured by temperature transducers and recorded. The temperature transducers were installed at the centre of the winding and end winding stacks to measure the hot spot temperatures. In the tests, air cooling was applied to the stator housing using a cooling fan with average air flow rate of 8.4 m/s. The ambient and coolant temperatures were measured and fed to the input $X$ in (35). Since the time of ambient temperature and coolant temperature changes is much longer than the prediction horizon, the $T_C$ and $T_E$ in $X$ were assumed to be equal and constant during the $N$ steps.

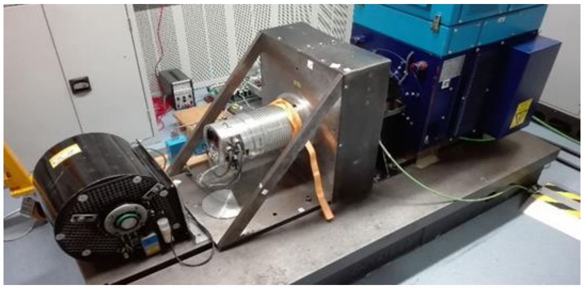

Fig. 9. Test rig.

The tests were performed with the maximum reference temperature set to 90 °C. It was deliberately set to a lower value than the winding rated temperature to assess how the proposed scheme responds to the thermal limit. $T_W(k)$ and $T_{EW}(k)$ in (31) for the model predictive block were the measured winding and end-winding temperatures. $T_{rot}(k)$ in (31) was set to the reference maximum temperature (90°C), therefore, the MPC was only minimizing the errors of $T_W(k)$ and $T_{EW}(k)$. The time step of the MPC was set to 10 s and the number of prediction steps, $N$, was set to 10. Indeed, $N$ is a tuning parameter of the MPC control. With a large $N$, the temperature correction action will be slower, and the reduction in the torque limit will be more gradual. The effect will be opposite if $N$ is small. In addition, since (30) is obtained from iterations, a larger $N$ may bring more errors to (30) due to the thermal model error, motor loss calculation error and the assumptions used to simplify the cost function in (37).

The proposed active thermal management was performed on an ADSP-TS201 digital signal processor (DSP). According to (35), the $Y$ in (36) should be calculated at every time step before the output of the MPC is updated and the calculation of $Y$ requires a $(N-1)^{th}$ order matrix multiplication, i.e., the calculation of $A_d^{N-1}$, which significantly increases the computational load. In order to decrease the computational load, $A_d^x$ is calculated based on $A_d^{x-1}$ which, in turn, is calculated in the previous execution of the main loop. In this way, the DSP only need to perform a 1st order matrix multiplication within one main loop execution. The resultant $A_d^x$ is added to $\sum_{j=0}^{x-1} A_d^{x-1}$ obtained in the previous main loop execution until $x$ increased to $N-1$. Therefore, the $\sum_{j=0}^{N-1} A_d^{N-j-1}$ can be obtained within $N$ main loop executions. After $\sum_{j=0}^{N-1} A_d^{N-j-1}$ is obtained, $Y$ can be calculated in one main loop execution and $P_{cu\_max}$ in (35) can be calculated in another main loop execution. Therefore, in the experiment, the update of the MPC output takes $(N+2)$ main loop executions. Since the motor temperature varies much more slowly than the execution time of the main loop, the update time is negligible.

Fig. 10 shows the reference torque, actual torque, torque limit profile generated by the MPC control and the measured motor speed. At the beginning, the motor is running at the speed of 1000 r/min and the reference torque is set to 65 Nm. As can be seen in Fig. 10, before t=500s, the actual torque is equal to the reference torque. After t=500s the actual torque begins to decrease due to the torque limit, $T_{e\_lim}$, which is imposed by the MPC thermal control scheme since the measured motor temperature increases. At t=1760 s, the reference torque is set to 10 Nm, and the motor speed decreases to 400 r/min at t=1790s.

Since the reference torque, e.g., 10 Nm, is smaller than the torque limit generated by MPC thermal control scheme, the actual torque follows the reference torque and the motor temperature decreases which allows for the increase of $T_{e\_lim}$. At t=2125 s, the reference torque increases to 65 Nm again and the speed is kept at 400 r/min. As can be seen in Fig. 10, the actual torque is limited by the MPC thermal control scheme again.

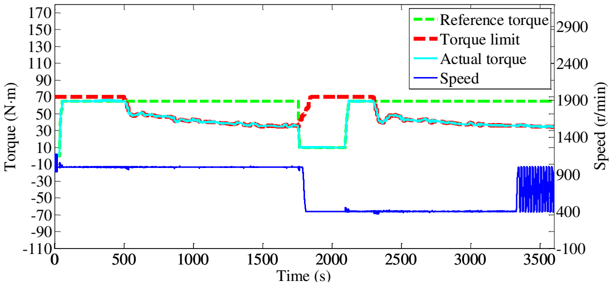

Fig. 10. Reference torque, actual torque, speed when reference maximum temperature is set to 90℃.

To study the speed influence on the MPC thermal control scheme, after t=3320 s, the motor speed was controlled to vary between 400 r/min and 1000 r/min every 20 s. As can be seen in Fig. 11, the MPC thermal control can still limit the actual torque effectively.

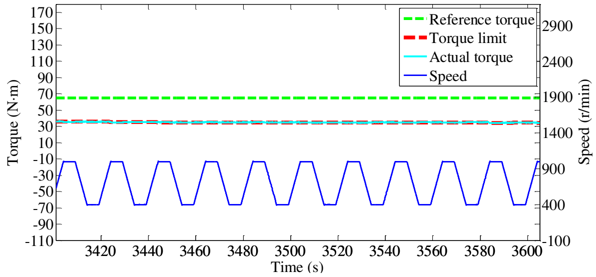

Fig. 11. The zoom in the speed variation between t=3400 s to 3600 s.

The resultant winding and end winding temperatures are shown in Fig. 12 along with the maximum reference temperature ($T_{e\_lim}$ in Fig. 2). As can be seen from Fig. 12, the average of the measured winding and end-winding temperatures are close to the maximum reference temperature. This is because the cost function in (35) minimizes the error of winding and end-winding temperatures. Therefore, the control performance of the proposed active thermal management has been validated.

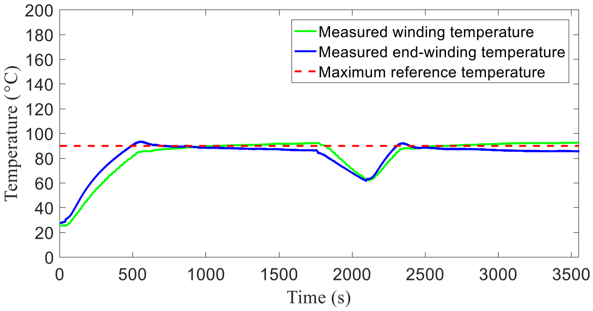

Fig. 12. The measured winding, end-winding temperatures and the maximum reference temperature.

## V. CONCLUSION

This paper has proposed an active thermal management control scheme based on a model predictive control concept. The performances of the proposed scheme have been assessed by simulations for EV traction over WLTC driving cycles and experiments with step changes in torque. In both cases, the winding temperatures can be effectively limited to a value close to the maximum reference temperature. It is shown that imposing a thermal limit results in deterioration of torque or speed tracking performance. Thus, a trade-off between the active thermal management and drive performance must be appreciated. In traction applications, imposing a thermal limit would reduce the torque capability and hence acceleration and maximum speed in adverse driving conditions in favour of lower temperature stress and longer lifetime.

## REFERENCES

[1] T. Sun, J. Wang, M. Koc, and X. Chen, “Self-Learning MTPA Control of Interior Permanent Magnet Synchronous Machine Drives Based on Virtual Signal Injection,” *IEEE Trans. Ind. Appl.*, vol. 52, no. 4, pp. 3062–3070, 2016.

[2] T. Sun, J. Wang, and M. Koc, “Virtual Signal Injection Based Direct Flux Vector Control of IPMSM Drives,” *IEEE Trans. Ind. Electron.*, vol. 63, no. 8, pp. 4773–4782, 2016.

[3] C. Sciascera, P. Giangrande, L. Papini, C. Gerada, and M. Galea, “Analytical Thermal Model for Fast Stator Winding Temperature Prediction,” *IEEE Trans. Ind. Electron.*, vol. 64, no. 8, pp. 6116–6126, 2017.

[4] C. Rhebergen *et al.*, “Enhancement of Electric Motor Thermal Management through Axial Cooling Methods: A Materials Approach,” in *Proc. ECCE.*

[5] *IEEE Guide for the Presentation of Thermal Limit Curves for Squirrel Cage Induction Machines*. .

[6] L. U. Gokdere, A. Bogdanov, S. L. Chiu, K. J. Keller, and J. Vian, “Adaptive Control of Actuator Lifetime,” in *Proc. IEEE AERO.*, 2006, pp. 1–11.

[7] F. Qi, A. Stippich, S. Koschik, and R. W. De Doncker, “Model Predictive Overload Control of Induction Motors,” in *Proc.IEEE IEMDC.*, 2015, pp. 999–1005.

[8] F. Qi, D. A. Ly, C. Van Der Broeck, D. Yan, and R. W. De Doncker, “Model Order Reduction Suitable for Online Linear Parameter-Varying Thermal Models of Electric Motors,” in *Proc.IEEE SPEC*, 2016, pp. 1–6.

[9] T. Sun, J. Wang, A. Griffo, and B. Sen, “Active Thermal Management for Interior Permanent Magnet Synchronous Machine ( IPMSM ) Drives,” in *Proc.IEEE IEMDC.*, 2017, pp. 1–8.

[10] F. Qi, I. Ralev, A. Stippich, and R. W. De Doncker, “Model Predictive Overload Control of an Automotive Switched Reluctance Motor for Frequent Rapid Accelerations,” in *Proc.ICEMS*, 2016, vol. 1, no. 1, pp. 1–6.

[11] F. Qi, I. Ralev, A. Klein-hessling, and R. W. De Doncker, “Online Temperature Estimation of an Automotive Switched Reluctance Motor Using Space-resolved Lumped Parameter Network,” in *Proc.ICEMS*, 2016, pp. 1–6.

[12] T. Sun, J. Wang, and X. Chen, “Maximum Torque per Ampere (MTPA) Control for Interior Permanent Magnet Synchronous Machine Drives Based on Virtual Signal Injection,” *IEEE Trans. Power Electron.*, vol. 30, no. 9, pp. 5036–5045, 2015.

[13] T. Sun and J. Wang, “Extension of Virtual Signal Injection Based MTPA Control for Interior Permanent Magnet Synchronous Machine Drives into Field Weakening Region,” *IEEE Trans. Ind. Electron.*, vol. 62, no. 11, pp. 6809–6817, 2015.

[14] T. Huber, W. Peters, and J. Böcker, “A Low-Order Thermal Model for Monitoring Critical Temperatures in Permanent Magnet Synchronous Motors,” in *Proc.IET PEMD.*, 2014, pp. 1–6.

[15] P. H. Mellor, R. Wrobel, and D. Holliday, “A Computationally Efficient Iron Loss Model for Brushless AC Machines that Caters for Rated Flux and Field Weakened Operation,” in *Proc.IEEE IEMDC.*, 2009, pp. 490–494.

[16] J. Goss, P. H. Mellor, R. Wrobel, D. A. Staton, and M. Popescu, "The Design of AC Permanent Magnet Motors for Electric Vehicles: A Computationally Efficient Model of The Operational Envelope," in *Proc. IET PEMD.*, 2012, pp. 1–6.

[17] X. Chen, J. Wang, and A. Griffo, "A High-Fidelity and Computationally Efficient Electro-thermally Coupled Model for Interior Permanent-Magnet Machines in Electric Vehicle Traction Applications," *IEEE Trans. Transp. Electrif.*, vol. 1, no. 4, pp. 336–347, 2015.

[18] C. Kral, A. Haumer, and S. Bin Lee, "A Practical Thermal Model for the Estimation of Permanent Magnet and Stator Winding Temperatures," *IEEE Trans. Power Electron.*, vol. 29, no. 1, pp. 455–464, 2014.

[19] M. Ganchev, B. Kubicek, and H. Kappeler, "Rotor Temperature Monitoring System," in *Proc.IEEE ICEM*, 2010, pp. 1–5.

[20] M. Kovacic, M. Vražic, and I. Gašparac, "Bluetooth Wireless Communication and 1-Wire Digital Temperature Sensors in Synchronous Machine Rotor Temperature Measurement," in *Proc.IEEE EPE-PEMC*, 2010, pp. 25–28.

[21] O. Wallscheid, S. Member, and B. Joachim, "Global Identification of a Low-Order Lumped-parameter Thermal Network for Permanent Magnet Synchronous Motors," *IEEE Trans. Energy Convers.*, vol. 31, no. 1, pp. 354–365, 2016.

**Tianfu Sun** (S'15–M'16) was born in China. He received B.Eng. degree in mechanical engineering, M.Sc. degree in civil engineering from Dalian University of Technology, Dalian, China, in 2009 and 2012, respectively and the Ph.D. degree in electrical and electronic engineering from the University of Sheffield, Sheffield, U.K., in 2016. From 2016 to 2017, he was with the Department of Electronic and Electrical Engineering, University of Sheffield, Sheffield, UK., where he was a Postdoctoral Research Fellow.

He is currently working as an Associate Professor in electric drives at Shenzhen Institutes of Advanced Technology, Chinese Academy of Sciences, Shenzhen, China. His current research interests include power electronics and the motor drives.

**Jiabin Wang** (S'94–A'96–M'01–SM'03) received the B.Eng. and M.Eng. degrees from Jiangsu University of Science and Technology, Zhenjiang, China, in 1982 and 1986, respectively, and the Ph.D. degree from the University of East London, London, U.K., in 1996, all in electrical and electronic engineering.

Currently, he is a Professor in Electrical Engineering at the University of Sheffield, Sheffield, U.K. From 1986 to 1991, he was with the Department of Electrical Engineering at Jiangsu University of Science and Technology, where he was appointed a Lecturer in 1987 and an Associated Professor in 1990. He was a Postdoctoral Research Associate at the University of Sheffield, Sheffield, U.K., from 1996 to 1997, and a Senior Lecturer at the University of East London from 1998 to 2001. His research interests range from motion control and electromechanical energy conversion to electric drives for applications in automotive, renewable energy, household appliances and aerospace sectors.

He is a fellow of the IET and a senior member of IEEE.

**Antonio Griffo** (M'13) received the M.Sc. degree in electronic engineering and the Ph.D. degree in electrical engineering from the University of Napoli "Federico II," Naples, Italy, in 2003 and 2007, respectively. From 2007 to 2013, he was a Research Associate with the University of Sheffield, Sheffield, U.K., and the University of Bristol, Bristol, U.K. He is currently a Lecturer with the Department of Electronic and Electrical Engineering, University of Sheffield. His research interests include modeling, control and condition monitoring of electric power systems, power electronics converters, and electrical motor drives, for renewable energy, automotive and aerospace applications.

**Bhaskar Sen** (M'17) received the B.E. degree from the Delhi College of Engineering, Delhi, India, in 2003, the M.Tech. degree from the Indian Institute of Technology, Kanpur, India, in 2006, both in electrical engineering, and the Ph.D. degree in electrical and electronic engineering from The University of Sheffield, Sheffield, U.K., in 2015. From 2006 to 2011, he was a Research Engineer with GE Global Research, Bangalore, India. From 2015 to 2017, he was a Research Associate at The University of Sheffield. His research interests include electrical machine fault modeling, machine fault detection, and fault-tolerant drives.